Ultrasonics Sonochemistry 91 (2022) 106223

Contents lists available at ScienceDirect

Ultrasonics Sonochemistry

journal homepage: www.elsevier.com/locate/ultson

Bi-MOFs with two different morphologies promoting degradation of organic dye under simultaneous photo-irradiation and ultrasound vibration treatment

Shanghai Dong, Liying Wang *, Weiyi Lou, Yunxin Shi, Zhenzhu Cao, Yongfeng Zhang, Junmin Sun

School of Chemical Engineering, Inner Mongolia University of Technology, Inner Mongolia Key Laboratory of Efficient Recycle Utilization for Coal-Based Waste, National & Local Joint Engineering Research Center of High-Value Utilization of Coal-Based Solid Waste, Institute of Coal Conversion and Cyclic Economy, Hohhot 010051, People's Republic of China

ARTICLE INFO

Keywords:
Bismuth-based MOFs
Piezo-photocatalysis
Piezoelectric property
Environmental remediation

ABSTRACT

For the first time, piezocatalysis activity has been observed in bismuth-based MOFs (ultrasound vibration treatment) with two different morphologies, namely FCAU-17 (flakes) and CAU-17 (rods). CAU-17 and FCAU-17 were synthesized by solvothermal and ultrasonic methods, respectively, with the same organic ligand (1,3,5-benzenetricarboxylic acid) and metal salt ($Bi(NO_3)_3{\cdot}5H_2O$). Among these, the apparent rate constant k of CAU-17 in piezo-photocatalysis is 3.9×10^{-2} min^{-1}, which is ~3.9 and ~ 1.5 times of those in photocatalysis and piezocatalysis, respectively. CAU-17 showed much high piezo-photocatalytic activity during degradation of RhB. Efficiently coupling between piezocatalysis and photocatalysis has been realized in rod-like CAU-17 (ultrasound vibration treatment). Our results provide a new strategy to improve catalytic performance of Bi MOFs through an efficient synergistic piezo-photocatalysis approach for environmental remediation.

1. Introduction

Environmental pollution and energy crisis hinder the sustainable development of human society. Photocatalysis is considered to be an effective solution to environmental pollution problems [1,2]. Nevertheless, the high recombination rate of photoinduced free electrons and holes severely restrains its catalytic activity [3,4]. In order to enhance the separation efficiency of photoexcited charges, the introduction of defects in the lattice, nanostructured morphology maneuvering, cocatalyst decoration and the formation of composite semiconductors, etc [5–9], have been developed. Among them, built-in electric field has been considered as a driving force to achieve better charges separation [10,11]. Piezo-photocatalysis, which is subject to both light irradiation and mechanical stress, has been a research priority [12,13].

A number of inorganic piezoelectric materials including $BaTiO_3$ [14], Bi_2WO_6 [15], BiOX (X = Cl, Br) [12,16,17], ZnO [13], $Bi_{0.5}Na_{0.5}TiO_3$ [18], $Ba(Zr_xTi_{1-x})O_3$ [19], $ZnSnO_3$ [20], UiO-66-NH2 (Hf) [21,22] have demonstrated notable catalytic activity. BiOCl catalyst decomposed 99% rhodamine B after lighting and vibrating for about 96 min, while 26% and 72% decomposition efficiencies were obtained with piezocatalysis only or photocatalysis only, respectively. The improved decomposition efficiency of piezo-photocatalysis was attributed to piezoelectric potential generated by the mechanical strain under vibrations, which increases the light-induced separation between electron-hole pairs [12]. The degradation efficiency of $Bi_{0.5}Na_{0.5}TiO_3$ (BNT) nanorods for RhB solution reached 95% within 30 min, and the decomposition performance of BNT nanorods significantly outdid that of nanospheres [18]. On the other hand, the different crystal face exposed by catalyst with different morphology has important influence on the decomposition reaction activity. Zihan Kang et al. synthesized BWO nanosheets with tunable Bi vacancies in a template hydrothermal method, the BWO nanosheets with the highest content of Bi vacancies exhibited significantly enhanced piezocatalytic degradation efficiency compared to RhB, which demonstrated the effect of metal oxygen vacancies on piezoelectric materials [23].

Recently, high hydrogen production activity of UiO-66-NH_2(Hf) has been achieved for the first time as the result of the strong piezoelectric response (ultrasound vibration treatment) [22]. A novel UiO-66(Zr)-F4 metal-organic framework (MOF) nanosheet for piezoelectric catalytic hydrolysis was fabricated by Shiyin Zhao et al. The hydrogen

* Corresponding author.
E-mail address: Wly2004@imut.edu.cn (L. Wang).

https://doi.org/10.1016/j.ultsonch.2022.106223
Received 18 August 2022; Received in revised form 1 November 2022; Accepted 2 November 2022
Available online 9 November 2022

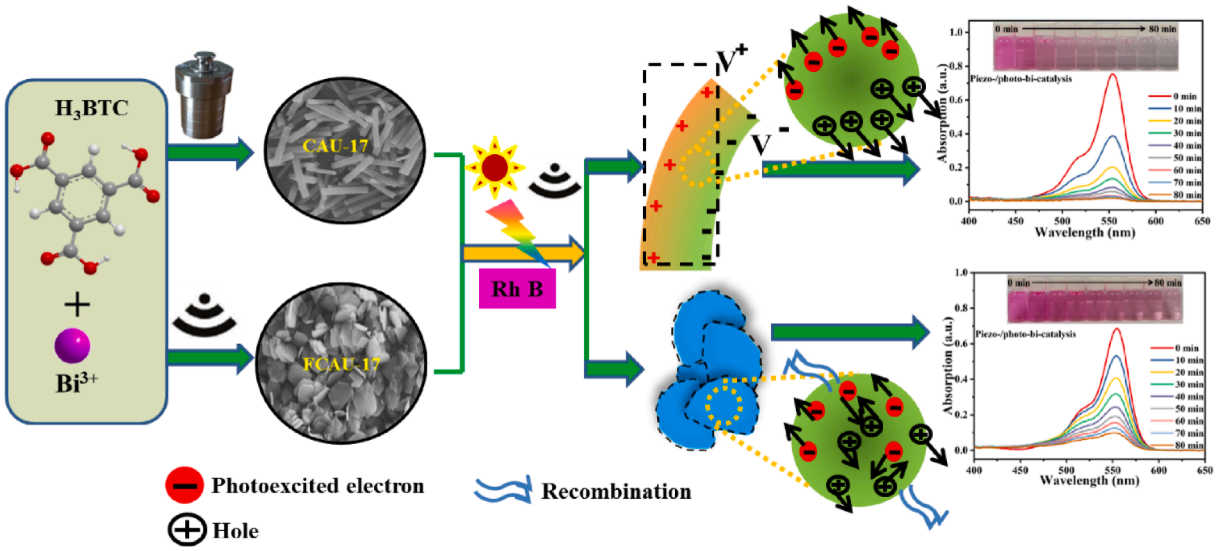

Fig. 10. Schematic illustration for the synthesis and piezo-photocatalysis of FCAU-17 (flakes) and CAU-17 (rods).

precipitation rate far exceeds that of the pristine UiO-66 host, which provides a feasible strategy for tuning the piezoelectricity of UiO-66 MOFs [24]. Compared with inorganic bismuth-based materials, Bi-MOFs have relatively low thermal and chemical stability, but the large pore size and surface area, certain unsaturated metal sites, and ease of design of bismuth-based metal-organic frameworks, all make Bi-MOFs a potentially good solid catalyst material [25–27]. However, there is no reports on the piezoelectric or piezo-photocatalysis of Bi MOF. To date, a more efficient synthetic approach to MOFs still remains a challenge. Compared with the high reaction temperature, high pressure, and long reaction time of hydrothermal, solvothermal, and microwave-assisted methods, ultrasonic synthesis is considered to be an efficient, low-cost, and environmentally friendly simple method for preparing MOFs [28,29]. In present study, the piezo-photocatalysis two different morphologies, FCAU-17 (flakes) and CAU-17 (rods)were studied (Scheme 1) for the first time. Results suggested that rod-like CAU-17 gives 96.7% decomposition efficiency in 80 min with the rate constant of 3.9×10^{-2} min^{-1} under simultaneous photo-irradiation and ultrasound vibration treatment.

2. Experimental

2.1. Materials

1,3,5-Benzenetricarboxylic acid (H_3BTC, 98%, Aladdin reagent Co., Ltd.), $Bi(NO_3)_3{\cdot}5H_2O$ (99%, Sinopharm Chemical Reagent Co., Ltd.) and Methanol 99.5%, Tianjin Fengchuan Chemical Reagent Technology Co., Ltd.) were used without further purification.

2.2. Preparation of samples

(1) Bi-MOFs-1 (FCAU-17) microflakes were synthesized under sonication. 0.42 g (2.0 mmol) 1,3,5-benzenetricarboxylic acid was dissolved in 50 mL methanol. Then 0.97 g (2.0 mmol) Bi $(NO_3)_3{\cdot}5H_2O$ was added to the solution and sonicated (40 kHz, 300 W) for 1 h.

(2) The Bi-MOFs-2 (CAU-17) microrods were synthesized with modifications according to the previous report [30]. 1,3,5-benzenetricarboxylic acid (0.42 g, 2.0 mmol) was dissolved in methanol (50 mL). Then $Bi(NO_3)_3{\cdot}5H_2O$ (0.97 g, 2.0 mmol)) was added to the solution. Afterwards, mixture was transferred to 100 mL teflon lined stainless steel reactor. The reactor was heated at 120 °C for 24 h.

2.3. Characterizations

The Bi-MOFs were measured by Fourier transform infrared spectroscopy (FTIR Tracer-100, SHIMADZU). X-ray diffraction (XRD, Smartlab-3KW + UltimaIV3KW, Cu Kα radiation) was used to characterize the crystal structure of the CAU-17 and FCAU-17 ($10°{\cdot}min^{-1}$ from 5° to 80°). The chemical states and surface chemical composition of the Bi-MOFs were characterized with an X-ray photoelectron spectroscopy (XPS, ESCALAB 250Xi, Thermo-Fisher, America). The specific surface area and structural parameters of the samples measured were obtained by N_2 adsorption-desorption method (BET, Quantachrome, USA) at 77 K (Fig. S1, Table S1). The structure and detailed morphology of the samples were obtained by scanning electron microscopy (SEM, HITACHI S-3400 N). Transmission electron microscopy (TEM) images were recorded on a FEI corporation G2 F30. The piezoelectric response of the samples was characterized by Bruker Multimode 8 piezoresponse force microscope (PFM, Germany). UV–vis adsorption spectra were carried out using a Shimadzu UV–vis spectrophotometer UV-3600. The total organic carbon (TOC, Shimadzu, Table S2) was determined by multi N/C 2100. The photoluminescence (PL) spectra were characterized by F-4500 fluorescence spectrometer (Hitachi, Japan) to obtain the separation efficiency of holes and electrons. The photoelectrochemical measurements were obtained by an electrochemical workstation (CHI760E) in a standard three-electrode system and 0.1 M Na_2SO_4 electrolyte solution. A saturated calomel reference electrode served as the reference electrode, Pt was used as the counter electrode and the working electrode was prepared by coating the catalyst on indium tin oxide (ITO) glass. The electron paramagnetic resonance (EPR) spectra were investigated on a Bruker model A300–10/12 spectrometer under photo-irradiation and ultrasound vibration.

2.4. Piezo-photocatalysis experiments

The piezo-photocatalytic property of CAU-17 and FCAU-17 were measured by decomposition of RhB. In the experiments, a xenon lamp (300 W, wavelength > 420 nm) as the illuminant and an ultrasonic cleaner (300 W, 40 kHz) to offer periodic ultrasonic vibrations. The experiments were conducted by adding 100 mg of catalyst to 5 mg/l of 100 ml rhodamine B solution in a 500 ml beaker at room temperature. The stirring speed was fixed for each experiment. The suspension was stirred continuously in the dark for 40 min prior to illumination and ultrasonic vibration to achieve adsorption-desorption equilibrium. Suspension of 3.0 ml was withdrawn every 10 min through a syringe during

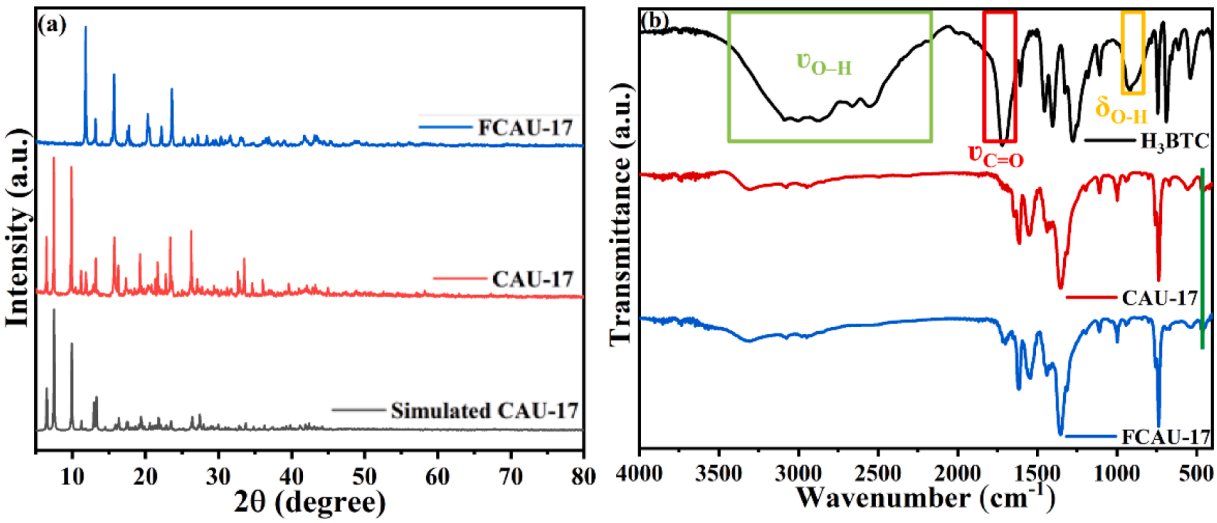

Fig. 1. XRD (a) pattern of the CAU-17 and FCAU-17; FT-IR (b) pattern of the CAU-17 and FCAU-17.

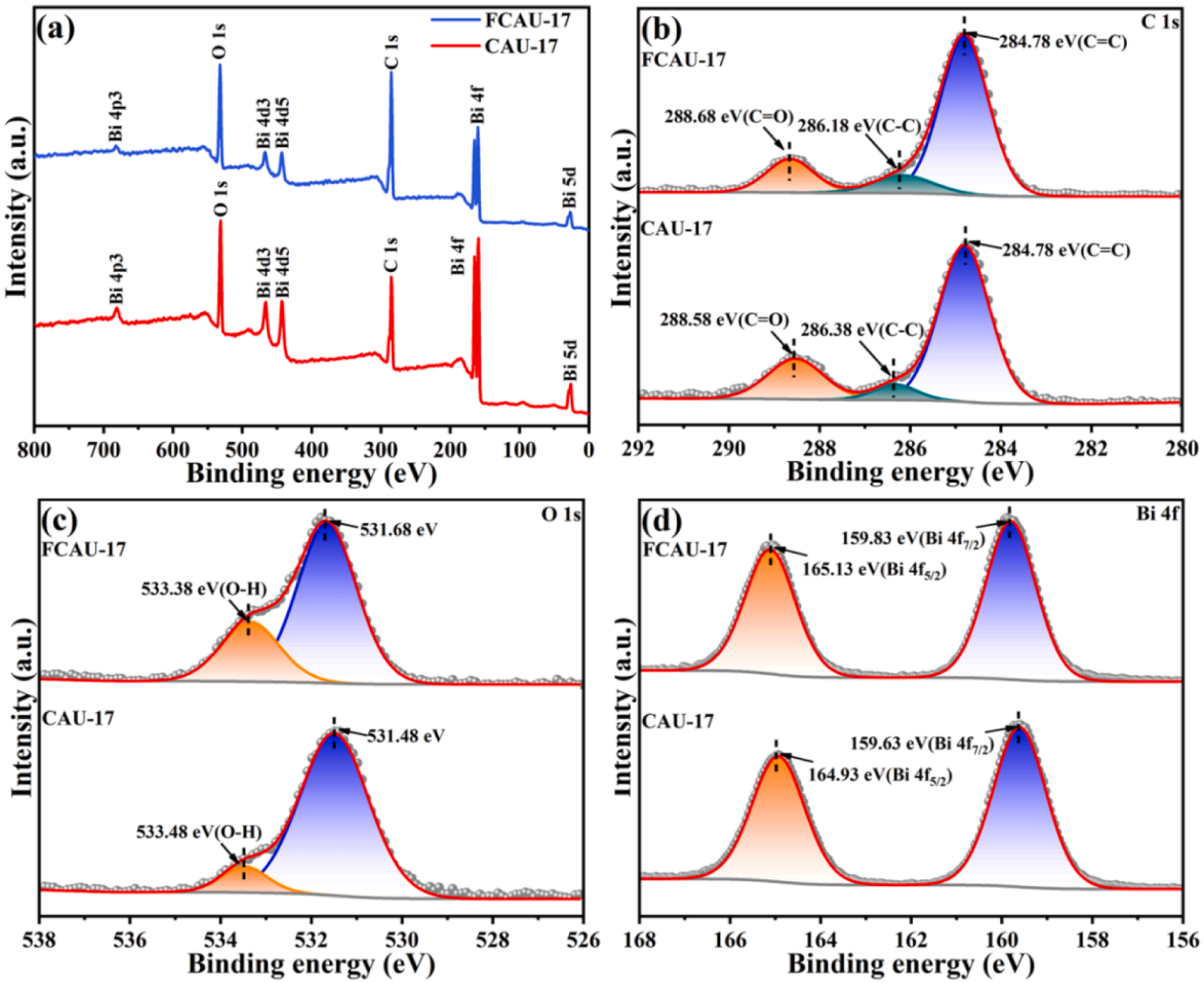

Fig. 2. XPS spectra of the FCAU-17 and CAU-17 in the: survey (a), C 1 s (b), O 1 s (c) and Bi 4f (d).

the degradation experiments. The concentration of dyes was analyzed by absorbance values at 553 nm with an UV–Vis spectrometer (UVT6, Purkinje General, China).

3. Results and discussion

3.1. Synthesis and characterization

The XRD patterns of CAU-17, FCAU-17and simulated CAU-17 are

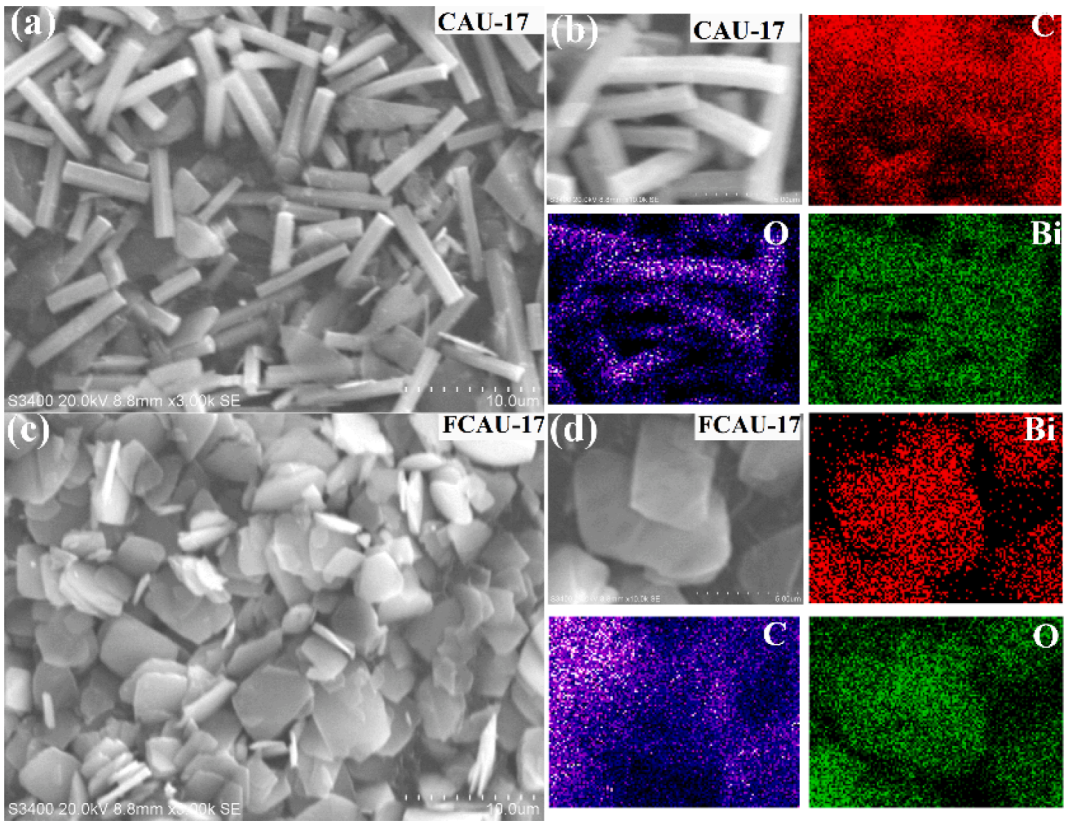

Fig. 3. SEM images (a) and EDS mapping images (b) of CAU-17; SEM images (c), and EDS mapping images (d) of FCAU-17.

shown in Fig. 1 (a). The pattern of CAU-17 is consistent with that previously reported [30,31]. Three main peaks around 6.46°, 7.46° and 9.86° corresponding to the (030), ($\bar{2}$40) and (11$\bar{1}$) face of CAU-17 (CCDC number: 1426169) [25]. The position of diffraction peaks in pattern FCAU-17 do not agree with that in the pattern CAU-17, indicating that the morphology of MOFs synthesized by ultrasonic method changes distinctly. On the other hand, the synthesis time in ultrasonic method has been decreased to 1 h compared with 22 in traditional solvothermal method [22], which indicates that ultrasonic method is an effective process to prepare MOF [32].

The infrared spectrum of H_3BTC was shown in Fig. 1(b), similar IR spectrum has been obtained for CAU-17 and FCAU-17. υ_{O-H} peak located at 3400–2200 cm^{-1}, $\upsilon_{C=O}$ peak located at 1730–1680 cm^{-1}, and δ_{O-H} peak located at 950–890 cm^{-1}. The FT-IR spectra of CAU-17 was consistent with the previous reports [33]. In the FT-IR spectra FCAU-17, the characteristic peaks associated with υ_{O-H}, δ_{O-H} of raw material H_3BTC disappeared and the characteristic peaks of the O-Bi-O group appeared at 400–500 cm^{-1}, which indicated that COOH of H_3BTC has coordinated with the Bi metal ionby electrostatic interaction [34]. The FT-IR spectrum of FCAU-17 agree with that in the pattern CAU-17, indicating that both the MOFs samples have the same functional groups.

The surface chemical composition and chemical status of CAU-17 and FCAU-17were measured by XPS. Fig. 2(a) shows the survey scans of CAU-17 and FCAU-17, which demonstrate the presence of C, O and Bi elements in both samples. The C 1 s (Fig. 2(b)) spectra at 284.78 eV, 286.18 eV and 288.68 eV correspond to C═C, C—C and C═O in FCAU-17, respectively [33]. The O 1 s (Fig. 2 (c)) peak of FCAU-17 appear at 531.68 and 533.38 eV, which are related with H_2O, and the O in bismuth−oxo clusters, respectively. The Bi 4f spectra of FCAU-17 (Fig. 2 (d)) is located at 159.83 eV (Bi $4f_{7/2}$) and 165.13 eV (Bi $4f_{5/2}$) with ΔE = Bi $4f_{5/2}$ − Bi $4f_{7/2}$ of 5.3 eV, implying the presence of Bi^{3+}ion [34,35]. Similar peaks could be observed for CAU-17 [26,36].

The crystallization, morphology and elemental distribution of CAU-17 and FCAU-17 were investigated (Fig. 3). As shown in Fig. 3 (a), CAU -17 (rod) is a hexagonal prism with a diameter of about 2.5 μm and a length of about 10.0 μm. This rod is close to literature 22, but larger than the previous rod of literature (about 1.2 μm in dimeter and 4.5 μm in length) [23]. This morphology difference should be ascribed to the different hold time at the designed temperature. In addition, Bi, O, and C elements were distributed uniformly in CAU-17 (Fig. 3b). By contrast, thin flake has been obtained in the ultrasonic synthesis. To our knowledge, this is the first report on the formation of Bi MOF flake by ultrasonic method. The diameter and thickness are 2-8um and 300–500 nm. This flake is larger and thicker than that (2.5 um diameter) synthesized in solvothermal method using anhydrous methanol [27].The flake shorten the way of charge diffusion to the surface. The EDS image indicates that the elements Bi, O and C are also uniformly distributed (Fig. 3d). Compared with the flake shape of FCAU-17, the thin rod of CAU-17 is more susceptible to be stretched or deformed by external mechanical vibration, which will generates the formation of piezoelectric potentials and thus induces band shift [14,18]. Fig. S3, 4 shows the TEM and HRTEM images of CAU-17 and FCAU-17.

3.2. *Piezoelectric and optical properties*

The piezoelectric response of FCAU-17 microflakes and CAU-17 microrods were characterized by the PFM of contact mode. Topographic images, piezoelectric response and phase diagrams of CAU-17 and FCAU-17 were showed Fig. 4 and Fig. S4, respectively. Both FCAU-17 and CAU-17 exhibit a very rough surface. The clear contrst in amplitude and phase indicate that there are different polarization in CAU-17 powder. CAU-17 show a stronger and clearer contrast compared to those of FCAU-17 in PFM amplitude and phase images, which implies that CAU-17 has a stronger ferroelectric property [37–39]. As shown in Fig. 4 (d) and Fig. S4 (d), typical amplitude-voltage butterfly loops were exhibited and well-defined 180° phase-reversal hysteresis loops are

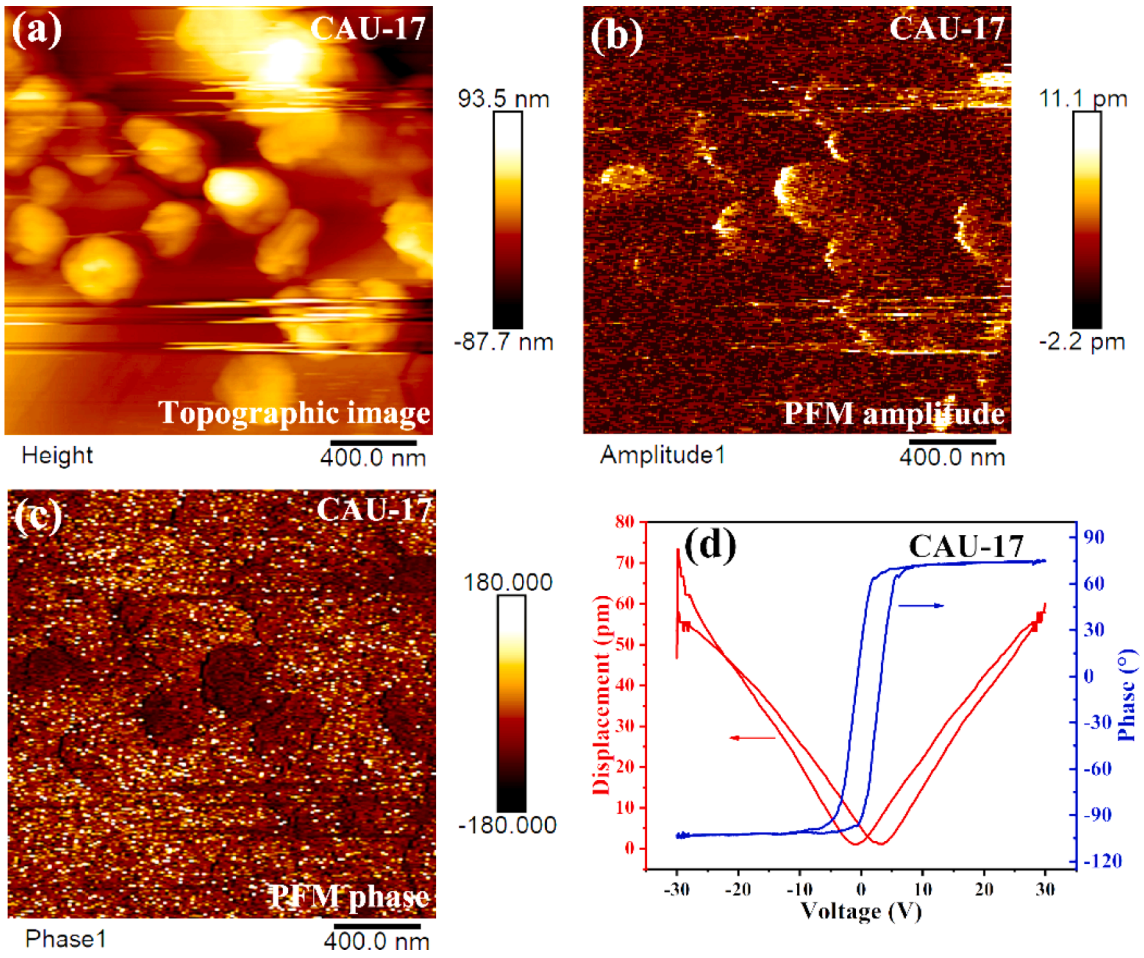

Fig. 4. Topography images (a), PFM amplitude (b) and phase images (c) of CAU-17 microrods. Amplitude-voltage butterfly loops and phase hysteresis loops (d) of CAU-17 microrods.

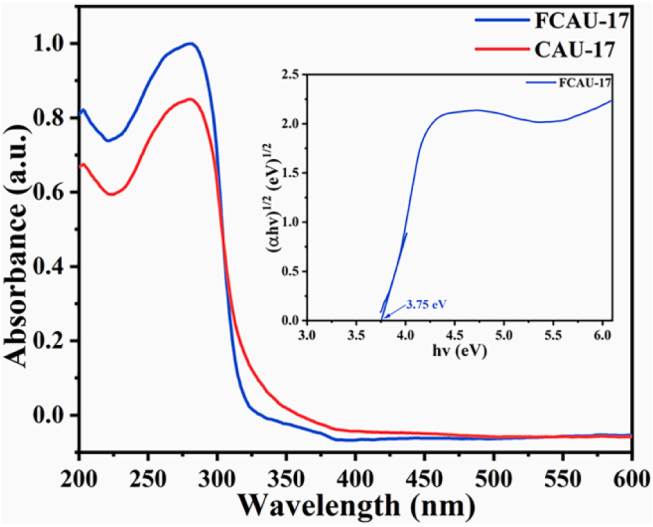

Fig. 5. UV–vis diffuse reflectance spectra of FCAU-17 and CAU-17; Plots of $(\alpha h\nu)^{1/2}$ against photon energy of FCAU-17.

obtained for both CAU-17 microrods and FCAU-17 microflakes. All ferroelectrics are piezoelectrics. This result justifies the piezoelectric nature of Bi-MOFs. The maximum PFM amplitude of CAU-17 microrods is nearly seven times higher than that of FCAU-17 microflakes [40]. Hence, the higher piezoelectric response of CAU-17 is more favorable for photo-induced electron-hole separation and has higher catalytic activity [17,41].

Light absorption properties are important for photocatalysis. UV–vis diffuse reflectance spectra (UV–vis DRS) of the FCAU-17 and CAU-17 were shown in Fig. 5. Both FCAU-17 and CAU-17 show strong absorption in the region of about 225–300 nm. The edge of the absorption band of FCAU-17 was around 317 nm. The band gaps (Eg) of FCAU-17 can be evaluated based on the Tauc's plots [42,43].

$$\alpha\,(h\nu) = A\,\left(h\nu - E_g\right)^{n/2} \quad (1)$$

where α is the absorption coefficient, h is Planck's constant, v is the light frequency, A is a constant, E_g is the band gap energy, and n is estimated from the optical transition of the semiconductor. According to Eq. (1), the band gap of FCAU-17 was estimated to be 3.75 eV. Similarly, the band gap of the prepared CAU-17 is estimated as ~3.83 eV [44,45].

3.3. Catalytic activity

As shown in Fig. 6 (a, c), the RhB removal efficiencies of single piezocatalysis, single photocatalysis and piezo-photocatalysis by FCAU-17 are 78.6%, 87.0% and 92.1%, respectively. On the other hand, the removal efficiencies of RhB by CAU-17 were 90.1%, 71.4% and 96.1%, respectively. Fig. 6 (b, d) shows that the catalytic process fits pseudo-first-order kinetic equations. Among these, the apparent rate constant k of CAU-17 in piezo-photocatalysis is 3.9×10^{-2} min^{-1} under simultaneous photo-irradiation and ultrasound vibration treatment, which is 1.5 and 3.9 times of those in bare piezocatalysis and photocatalysis,

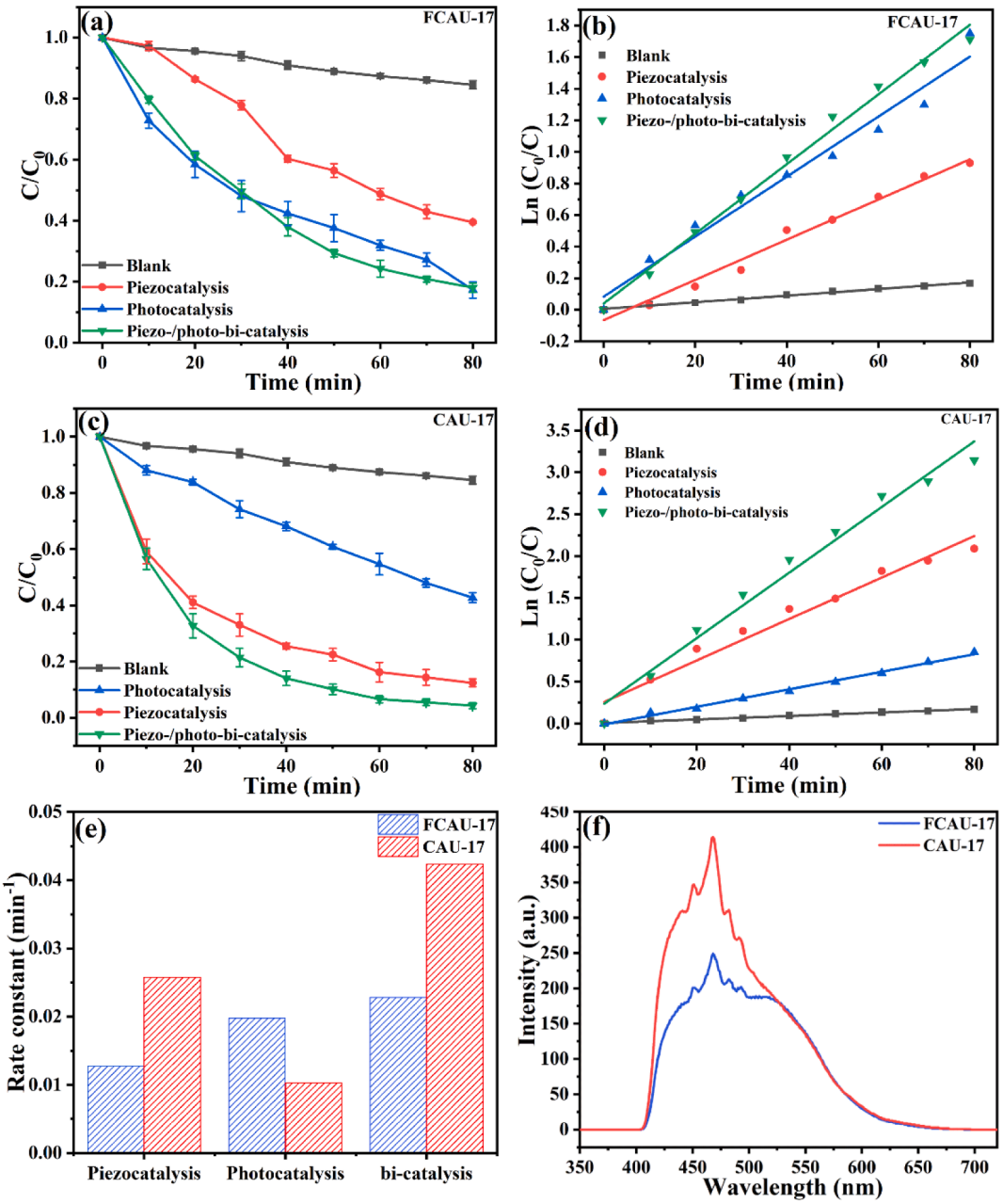

Fig. 6. Degradation efficiency of RhB (a) and the fitted kinetics (b) of FCAU-17 under different conditions. Degradation efficiency of RhB (c) and the fitted kinetics (d) of CAU-17 under different conditions. Comparison of the rate constant k (e) in the presence of FCAU-17 and CAU-17. Photoluminescence spectra (f) of FCAU-17 and CAU-17.

respectively. It should be stressed that notable piezoelectric catalytic activity have been observed for the first time. The higher piezocatalysis of rod-like CAU-17 could be ascribed to the easily deformed nature compared with FCAU-17 flake [14,46]. On the other hand, the larger size of CAU-17 might have more recombination of electron and hole than FCAU-17, which leads to its relatively low catalytic activity under irradiation of light. The higher intensity of PL peak indicates the high recombination of electron and hole in semiconductor. Fig. 6 (f) verify that the FCAU-17 can enhance effectively the separation rate of the photogenerated electron–hole pairs. It can be explained by the shorter diffusion distance to the plate surface.

Under the combination of ultrasound and light, the piezoelectric potential built in CAU-17 boost the e-h separation and further enhance the bi-catalytic activity (96.1%). However, the stiffness of FCAU-17 might only produce much weak synergetic effect and the no further increase of bi-catalytic has been achieved.

The UV–vis absorption spectra of CAU-17 and FCAU-17 catalysts during the degradation of RhB were shown in Fig. 7. Apparently, the characteristic absorption wavelength of RhB is at 553 nm. As shown in Fig. 7 (a, b), FCAU-17 exhibited slightly higher photocatalytic efficiency than CAU-17 due to the higher separation rate of photoexcited electron–hole pairs in FCAU-17 (Fig. 6f). However, CAU-17 exhibited higher piezocatalytic activity than FCAU-17 under ultrasound vibration treatment (Fig. 7 c and d). This higher piezocatalytic activity of CAU-17 might originate from the large piezoelectric potential, as the micro-rods are easily deformed [14,46].

In particular, RhB could be effectively degraded by the CAU-17 under synergism ultrasound vibration and photo-irradiation (Fig. 7 (e, f)). The enhanced bicatalysis activity could be attributed to the more effective synergetic effect between photocatalysis and piezocatalysis in

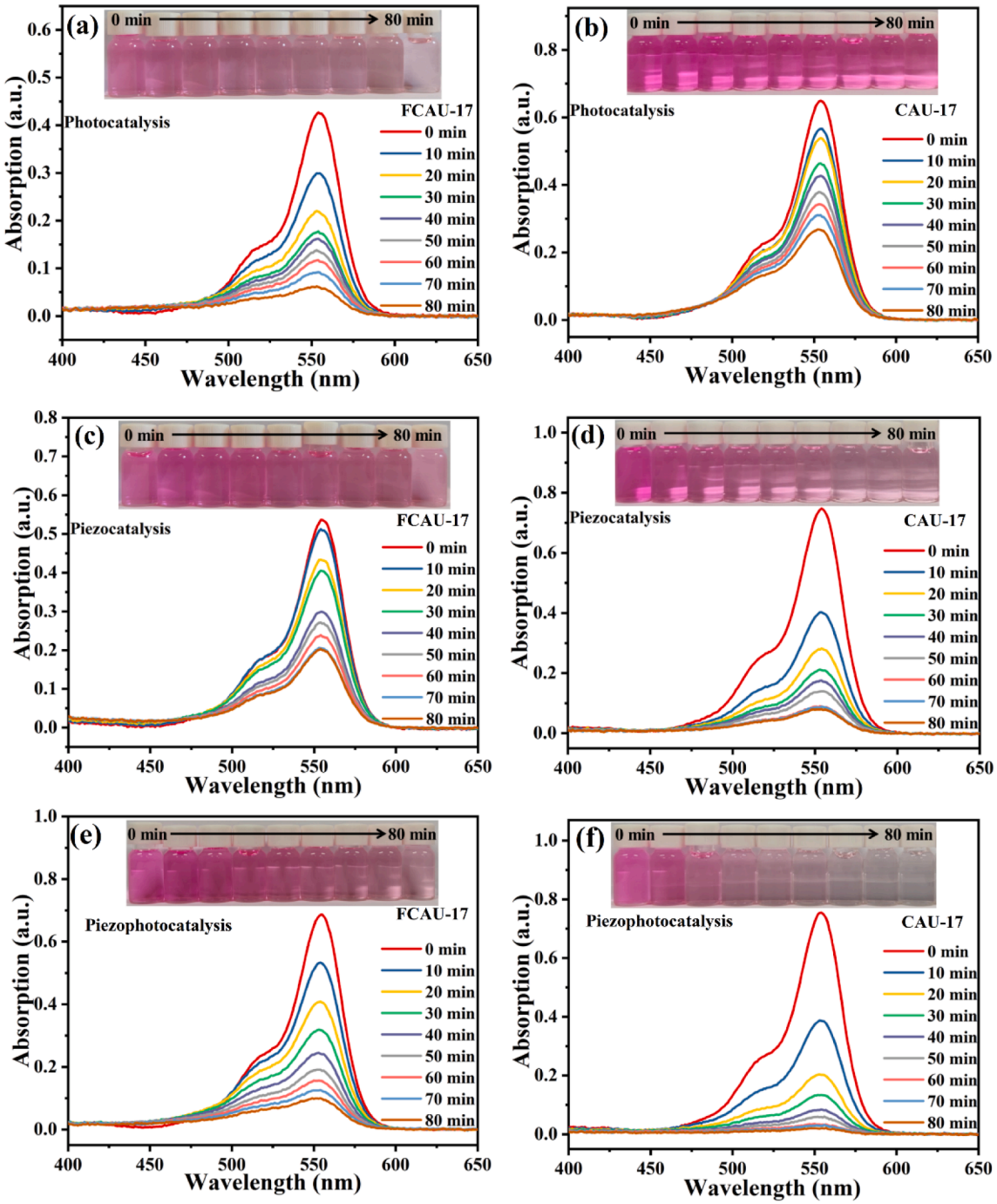

Fig. 7. Under different conditions, UV–Vis absorption spectra of RhB aqueous solutions for FCAU-17 (a, c, e) and CAU-17 (b, d, f).

deformable CAU-17 microrods.

Active species are important to understand the degradation mechanism. In addition, EPR measurement was used to detect •OH and $\bullet O_2^-$ radicals over the CAU-17 under simultaneous photo-irradiation and ultrasound vibration treatment. As shown in Fig. 8 (a, b), six characteristic peaks of DMPO-$\bullet O_2^-$ can be found after the light irradiation. The intensity ratio of 1:2:2:1 can be classified as the characteristic peaks of DMPO-•OH. The peak intensities increased with the irradiation. Consequently, it can be concluded that the •OH and $\bullet O_2^-$ radicals play important roles in the photocatalytic degradation of RhB. The higher photocurrent density of FCAU-17 than CAU-17 implies stronger charge separation efficiency than CAU-17 (Fig. 8 c). This is consistent with PL results (Fig. 6 f). On the other hand, the EIS plot of FCAU-17 shows a smaller arc than that of CAU-17 (Fig. 8 d), indicating a higher conductivity and a faster catalytic rate, which can well explain the decay catalytic activity in Fig. 6.

The band structure of CAU-17 was important for the piezo-photocatalysis mechanism. Although the band gap of the prepared CAU-17 is ~3.83 eV, which is difficult to absorb the visible light [44,47], RhB molecules can respond to visible light [48]. Thus, under visible light, the catalytic system photoresponse of CAU-17 was extended to the visible region by photosensitization. The photo-induced electrons are transferred from the RhB molecule to the conduction band of CAU-17 [12,49,47]. These electrons in the conduction band of CAU-17 react with oxygen molecules to generate reactive substances that further oxidize the RhB molecules(Fig. S6) [48]. Under ultrasonic

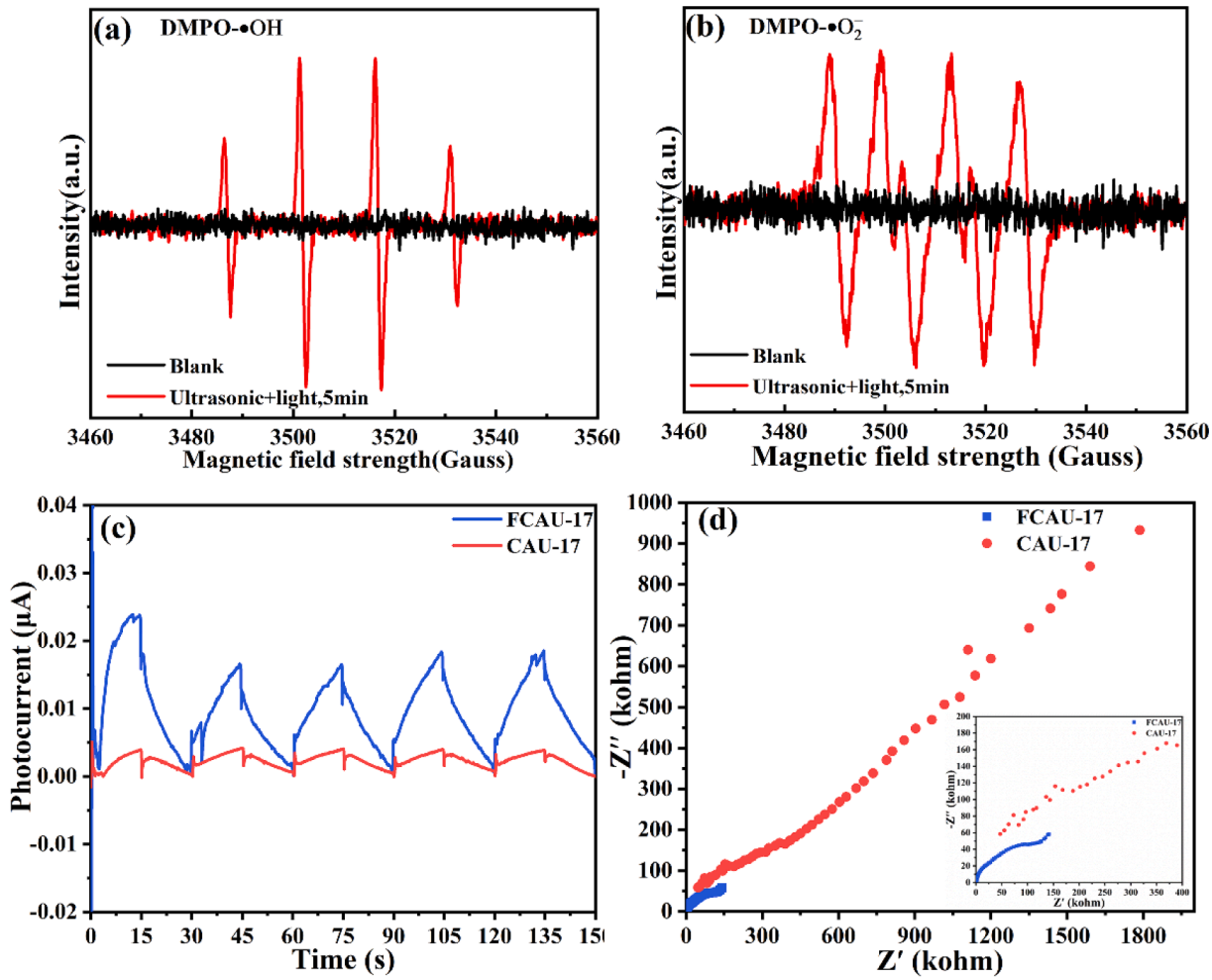

Fig. 8. EPR spectra of •OH and $•O_2^-$ radicals (a) over CAU-17 under simultaneous photo-irradiation and ultrasound vibration treatment. Photocurrent responses (b) and EIS plots (c) of the CAU-17.

condition, CAU-17 was subjected to periodic stress, and its internal electric field changes as shown in Scheme 1. The conduction band (CB) and valence band (VBM) potentials of CAU-17 are −1.8 eV and 2.03 eV, respectively [44]. The CB of CAU-17 (−1.8 eV vs. NHE) was much more negative than the standard redox potential of $O_2/•O_2^-$ (−0.33 eV vs. NHE) [14]. However, the high degree of photoexcitation charges recombination in the catalyst reduces the catalytic activity of CAU-17 [46]. Under ultrasonic vibration conditions, the catalyst was deformed due to the pressure generated by the break of cavitation bubble (Scheme 1). Therefore, a piezoelectric field was established in CAU-17. Simultaneously, the conduction band and valence band are both tilted by the piezoelectric potential [50]. The larger piezoelectric potential in CAU-17 assists the electrons and holes easier and faster in reacting with dissolved O_2 and OH^- to form $•O_2^-$ and •OH radicals.

Under ultrasound, CAU-17 was subjected to periodic stress, and its internal electric field changes as shown in Fig. 9. As shown in Fig. 9 (a), the CBM of CAU-17 (−1.8 eV vs. NHE) was much more negative than the standard redox potential of $O_2/•O_2^-$ (−0.33 eV vs. NHE) [14], so that the CBM electrons could be transported to the solution, enabling the reduction of dissolved O_2 to generate $•O_2^-$ radicals. On the other hand, the VBM of CAU-17 (+2.03 eV vs. NHE) was more positive than the standard redox potential of $OH^-/•OH$ (+1.9 eV vs. NHE) [14], thus allow the oxidation of OH^- by VB holes to generate •OH radicals. However, the high degree of photoexcitation charges recombination in the catalyst reduces the catalytic activity of CAU-17 without ultrasound-induced piezoelectric polarization [46]. Under ultrasonic vibration conditions, the catalyst was deformed due to the pressure generated by the break of cavitation bubble (Fig. 9 (b)). Therefore, a piezoelectric field was established in CAU-17. Driven by the piezoelectric potential, the free electrons and holes within the CAU-17 were attracted in opposite directions towards the crystal surfaces. Simultaneously, the conduction band and valence band are both tilted by the piezoelectric potential [50]. The larger piezoelectric potential in CAU-17 assists the electrons and holes easier and faster in reacting with dissolved O_2 and OH^- to form $•O_2^-$ and •OH radicals. As the accumulated screen charges are high enough to counteract the polarization charges within CAU-17, the driving force for charge separation would disappear and the redox reactions on the surface would be retarded (Fig. 9 (c)). The decrease in polarization upon falling ultrasound-induced pressure will break the potential equilibrium, leading to reverse charge transfer and new redox reactions (Fig. 9 (d)).

The stability and reusability of catalyst are of great importance for practical application. As shown in Fig. S5a, the degradation efficiency of CAU-17 for RhB could still be maintained at 65.0% after three cycles, indicating that CAU-17 maintained good piezo-photocatalytic activity for long-term reuse. The IR results of the used CAU-17 are similar the IR spectrum of the fresh 25-T/B (Fig. S5b). No extra diffraction peaks are observed in XRD pattern (Fig. S3. All results indicated that the CAU-17 has an excellent stability.

Recently, some Bi-MOFs have been investigated as novel photocatalyst. As seen from Table 1, notable photocatalytic activity for dye degradation has been achieved. However, CAU-17 catalyst shows

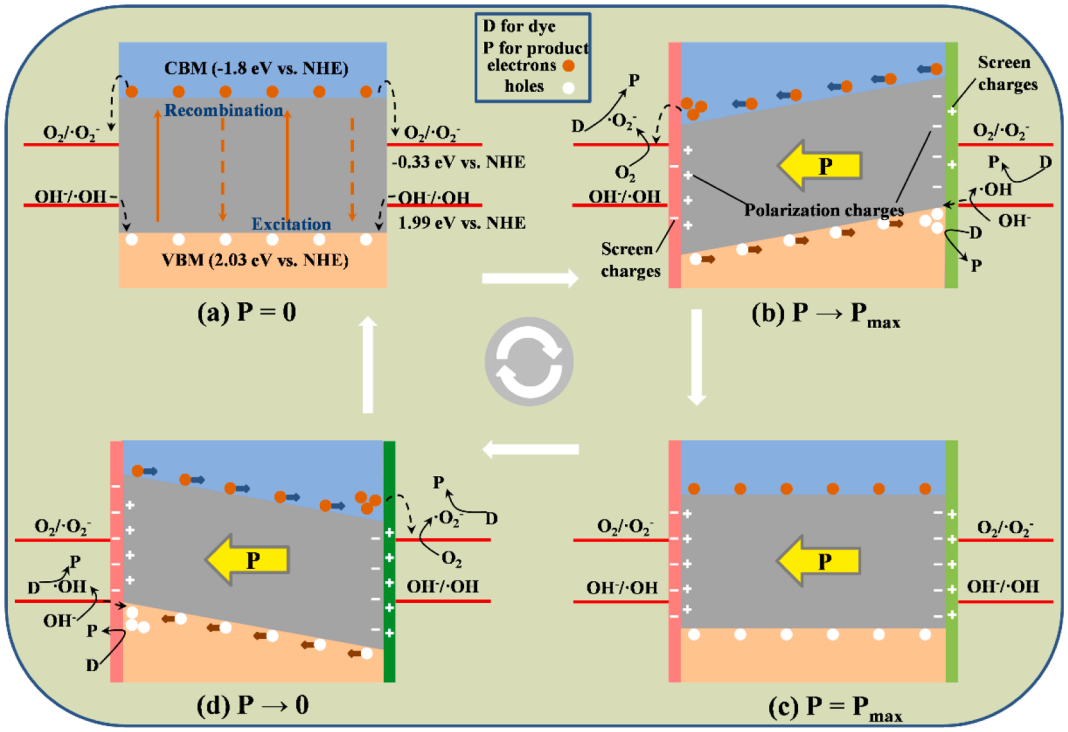

Fig. 9. Schematic illustration of the alternating internal electric field in B CAU-17 microrods during the ultrasonic treatment.

Table 1
List of photocatalytic degradation of dye by Bi MOF.

MOF	Irraidation source	Catalyst (mg/100 ml)	Dye (mg/L)	Effect (%)	Ref
Bi-mna	300 W Xe (>420 nm)	100	RhB 20 with oxygen	100 (120 min)	[51]
[Bi(BTC)(H2O)2]·H2O}*n*	120 W (UV 365 nm)	60	MO 10	35 (60 min)	[52]
Bi-FMOF	UV–vis radiation	33.3	CR 25	65 (30 min)	[53]
Bi-BDC	UV–vis radiation H_2O_2	100	CBB 10	97.61 (60 min)	[54]
FCAU-17	300 W Xe (>420 nm)	100	RhB	83.7 (80 min)	This work
CAU-17	300 W Xe (>420 nm) + ultrasonic (300 W)	100	RhB 5	97.2 (80 min)	This work

superior activity to other Bi MOF under th visible light without oxygen. It should be stressed that the piezocatalytic activity has been firstly reported in present study.

4. Conclusion

In summary, piezocatalysis has been observed in Bi MOF with different morphology for the first time. The rod like CAU-17 shows more effective synergetic effect between piezocatalysis and photocatalysis due to its stronger piezoelectric response as the result of its easily deformed nature. The rate constant k of CAU-17 in piezo-photocatalysis was 3.9×10^{-2} min^{-1}, which was 3.9 and 1.5 times higher than that of photocatalysis and piezoelectric photocatalysis, respectively. The piezoelectric potential in Bi MOF facilitates the efficient separation of electron and hole, which can boost the bicatalytic activity. Results indicates that CAU-17 is promising biocatalysts for dye degradation.

Declaration of Competing Interest

We have no known competing financial interests or personal relationships that could influence the work reported in this paper.

Data availability

Data will be made available on request.

Acknowledgments

This work was financially supported by the National Science Foundation of China (21762031), Program for Young Talents of Science and Technology of Inner Mongolia Autonomous Region (NJYT-20-A18), the Science Foundation of Inner Mongolia Autonomous Regions (2022MS02006) and Supported by Program for Innovative Research Team in Universities of Inner Mongolia Autonomous Region (NMGIRT2214).

Appendix A. Supplementary data

Supplementary data to this article can be found online at https://doi.org/10.1016/j.ultsonch.2022.106223.

References

[1] Q. Wang, K. Domen, Particulate photocatalysts for light-driven water splitting: mechanisms, challenges, and design strategies, Chem. Rev. 120 (2020) 919–985.
[2] J. Ran, J. Zhang, J. Yu, et al., Earth-abundant cocatalysts for semiconductor-based photocatalytic water splitting, Chem. Soc. Rev. 43 (2014) 7787–7812.
[3] C. Cheng, B. He, J. Fan, et al., An inorganic/organic S-scheme heterojunction H2-production photocatalyst and its charge transfer mechanism, Adv. Mater. 33 (2021), e2100317.
[4] K. Sun, M. Liu, J. Pei, et al., Incorporating transition-metal phosphides into metal-organic frameworks for enhanced photocatalysis, Angew. Chem. Int. Ed. Eng. 59 (2020) 22749–22755.

[5] F. Chen, Z. Ma, L. Ye, et al., Macroscopic spontaneous polarization and surface oxygen vacancies collaboratively boosting CO2 photoreduction on BiOIO3 single crystals, Adv. Mater. 32 (2020), e1908350.
[6] J. Bian, Z. Zhang, J. Feng, et al., Energy platform for directed charge transfer in the Cascade Z-scheme heterojunction: CO2 photoreduction without a cocatalyst, Angew. Chem. Int. Ed. Eng. 60 (2021) 20906–20914.
[7] Q. Guo, F. Liang, X.-Y. Gao, et al., Metallic Co2C: a promising co-catalyst to boost photocatalytic hydrogen evolution of colloidal quantum dots, ACS Catal. 8 (2018) 5890–5895.
[8] M. Xu, D. Li, K. Sun, et al., Interfacial microenvironment modulation boosting electron transfer between metal nanoparticles and MOFs for enhanced photocatalysis, Angew. Chem. Int. Ed. Eng. 60 (2021) 16372–16376.
[9] S. Yang, D. Fan, W. Hu, et al., Elucidating charge separation dynamics in a hybrid metal–organic framework photocatalyst for light-driven H2 evolution, J. Phys. Chem. C 122 (2018) 3305–3311.
[10] Z. Liang, C.-F. Yan, S. Rtimi, et al., Piezoelectric materials for catalytic/photocatalytic removal of pollutants: recent advances and outlook, Appl. Catal. B 241 (2019) 256–269.
[11] Y. Guo, W. Shi, Y. Zhu, Internal electric field engineering for steering photogenerated charge separation and enhancing photoactivity, EcoMat. 1 (2019), e12007.
[12] M. Ismail, Z. Wu, L. Zhang, et al., High-efficient synergy of piezocatalysis and photocatalysis in bismuth oxychloride nanomaterial for dye decomposition, Chemosphere. 228 (2019) 212–218.
[13] J. Ma, J. Ren, Y. Jia, et al., High efficiency bi-harvesting light/vibration energy using piezoelectric zinc oxide nanorods for dye decomposition, Nano Energy 62 (2019) 376–383.
[14] J. Wu, N. Qin, D. Bao, Effective enhancement of piezocatalytic activity of BaTiO3 nanowires under ultrasonic vibration, Nano Energy 45 (2018) 44–51.
[15] Z. Kang, N. Qin, E. Lin, et al., Effect of Bi2WO6 nanosheets on the ultrasonic degradation of organic dyes: roles of adsorption and piezocatalysis, J. Clean. Prod. 261 (2020), 121125.
[16] L. Li, M.A. Boda, C. Chen, et al., BiOBr micro–nanosheets: controllable synthesis and piezoelectric and photoelectric properties, Cryst. Growth Des. 21 (2021) 7179–7185.
[17] H. Lei, H. Zhang, Y. Zou, et al., Synergetic photocatalysis/piezocatalysis of bismuth oxybromide for degradation of organic pollutants, J. Alloys Compd. 809 (2019), 151840.
[18] X. Zhou, Q. Sun, D. Zhai, et al., Excellent catalytic performance of molten-salt-synthesized Bi0.5Na0.5TiO3 nanorods by the piezo-phototronic coupling effect, Nano Energy 84 (2021), 105936.
[19] M. Zhu, S. Li, H. Zhang, et al., Diffused phase transition boosted dye degradation with Ba (ZrxTi1−x)O3 solid solutions through piezoelectric effect, Nano Energy 89 (2021), 106474.
[20] A. Biswas, S. Saha, N.R. Jana, ZnSnO3 nanoparticle-based piezocatalysts for ultrasound-assisted degradation of organic pollutants, ACS Appl. Nano Mater. 2 (2019) 1120–1128.
[21] Y. Sun, J. Gao, Y. Cheng, et al., Design of the hybrid metal–organic frameworks as potential supramolecular piezo-/ferroelectrics, J. Phys. Chem. C 123 (2019) 3122–3129.
[22] C. Zhang, D. Lei, C. Xie, et al., Piezo-photocatalysis over metal-organic frameworks: promoting photocatalytic activity by piezoelectric effect, Adv. Mater. 33 (2021) 2106308.
[23] Z. Kang, E. Lin, N. Qin, et al., Bismuth vacancy-mediated quantum dot precipitation to trigger efficient piezocatalytic activity of Bi2WO6 nanosheets, ACS Appl. Mater. Interfaces 14 (2022) 11375–11387.
[24] S. Zhao, M. Liu, Y. Zhang, et al., Harvesting mechanical energy for hydrogen generation by piezoelectric metal-organic frameworks, Mater. Horiz. 9 (2022) 1978–1983.
[25] A.K. Inge, M. Koppen, J. Su, et al., Unprecedented topological complexity in a metal-organic framework constructed from simple building units, J. Am. Chem. Soc. 138 (2016) 1970–1976.
[26] W. Chai, W. Yin, K. Wang, et al., Carbon-coated bismuth nanospheres derived from Bi-BTC as a promising anode material for lithium storage, Electrochim. Acta 325 (2019), 134927.
[27] F. Li, G.H. Gu, C. Choi, et al., Highly stable two-dimensional bismuth metal-organic frameworks for efficient electrochemical reduction of CO2, Appl. Catal. B 277 (2020), 119241.
[28] Z.-Q. Li, L.-G. Qiu, T. Xu, et al., Ultrasonic synthesis of the microporous metal–organic framework Cu3(BTC)2 at ambient temperature and pressure: an efficient and environmentally friendly method, Mater. Lett. 63 (2009) 78–80.
[29] Z. Ma, D. Wu, X. Han, et al., Ultrasonic assisted synthesis of Zn-Ni bi-metal MOFs for interconnected Ni-N-C materials with enhanced electrochemical reduction of CO2, J. CO2 Util. 32 (2019) 251–258.
[30] H. Ouyang, N. Chen, G. Chang, et al., Selective capture of toxic selenite anions by bismuth-based metal-organic frameworks, Angew. Chem. Int. Ed. Eng. 57 (2018) 13197–13201.
[31] J. Chen, X. Chen, X. Zhang, et al., Nanostructured BiVO4 derived from bi-MOF for enhanced visible-light photodegradation, Chem. Res. Chin. Univ. 36 (2020) 120–126.
[32] C. Vaitsis, G. Sourkouni, C. Argirusis, Metal organic frameworks (MOFs) and ultrasound: a review, Ultrason. Sonochem. 52 (2019) 106–119.
[33] S.-R. Zhu, M.-K. Wu, W.-N. Zhao, et al., In situ growth of metal–organic framework on BiOBr 2D material with excellent photocatalytic activity for dye degradation, Cryst. Growth Des. 17 (2017) 2309–2313.
[34] H.-T.T. Nguyen, K.-N.T. Tran, L. Van Tan, et al., Microwave-assisted solvothermal synthesis of bimetallic metal-organic framework for efficient photodegradation of organic dyes, Mater. Chem. Phys. 272 (2021), 125040.
[35] M. Guo, Y. Wang, Q. He, et al., Enhanced photocatalytic activity of S-doped BiVO4photocatalysts, RSC Adv. 5 (2015) 58633–58639.
[36] J. Sun, L. Sun, S. Bai, et al., Pyrolyzing Co/Zn bimetallic organic framework to form p-n heterojunction of Co3O4/ZnO for detection of formaldehyde, Sensors Actuators B Chem. 285 (2019) 291–301.
[37] A. Zhang, Z. Liu, B. Xie, et al., Vibration catalysis of eco-friendly Na0.5K0.5NbO3-based piezoelectric: an efficient phase boundary catalyst, Appl. Catal. B 279 (2020), 119353.
[38] Z. Zhao, L. Wei, S. Li, et al., Exclusive enhancement of catalytic activity in Bi0.5Na0.5TiO3nanostructures: new insights into the design of efficient piezocatalysts and piezo-photocatalysts, J. Mater. Chem. A 8 (2020) 16238–16245.
[39] H. You, X. Ma, Z. Wu, et al., Piezoelectrically/pyroelectrically-driven vibration/cold-hot energy harvesting for mechano−/pyro- bi-catalytic dye decomposition of NaNbO3 nanofibers, Nano Energy 52 (2018) 351–359.
[40] N.P. Maria Joseph Raj, N.R. Alluri, G. Khandelwal, et al., The morphotropic phase boundary based BCST ferroelectric system for water remediation through bi-catalytic activity, J. Alloys Compd. 871 (2021), 159503.
[41] H. Lei, Q. He, M. Wu, et al., Piezoelectric polarization promoted spatial separation of photoexcited electrons and holes in two-dimensional g-C3N4 nanosheets for efficient elimination of chlorophenols, J. Hazard. Mater. 421 (2021), 126696.
[42] Q. Huang, Y. Hu, Y. Pei, et al., In situ synthesis of TiO2@NH2-MIL-125 composites for use in combined adsorption and photocatalytic degradation of formaldehyde, Appl. Catal. B 259 (2019), 118106.
[43] A. Crake, K.C. Christoforidis, A. Gregg, et al., The effect of materials architecture in TiO2 /MOF composites on CO2 photoreduction and charge transfer, Small. 15 (2019), e1805473.
[44] L. Yang, Y. Xin, C. Yao, et al., In situ preparation of Bi2WO6/CAU-17 photocatalyst with excellent photocatalytic activity for dye degradation, J. Mater. Sci. Mater. Electron. 32 (2021) 13382–13395.
[45] S. Dong, L. Wang, W. Lou, et al., Synthesis of TiO2/Bi-MOFs composites with excellent performance for enhanced visible-light driven photocatalytic activity to remove organic contaminants, J. Dispers. Sci. Technol. 1-12 (2022).
[46] J. Chen, H. Lei, S. Ji, et al., Synergistic catalysis of BiOIO3 catalyst for elimination of organic pollutants under simultaneous photo-irradiation and ultrasound-vibration treatment, J. Colloid Interface Sci. 601 (2021) 704–713.
[47] J. Jiang, K. Zhao, X. Xiao, et al., Synthesis and facet-dependent photoreactivity of BiOCl single-crystalline nanosheets, J. Am. Chem. Soc. 134 (2012) 4473–4476.
[48] C. Chen, W. Ma, J. Zhao, Semiconductor-mediated photodegradation of pollutants under visible-light irradiation, Chem. Soc. Rev. 39 (2010) 4206–4219.
[49] S. Singh, H. Mahalingam, P.K. Singh, Polymer-supported titanium dioxide photocatalysts for environmental remediation: a review, Appl. Catal. A 462–463 (2013) 178–195.
[50] S.C. Rai, K. Wang, J. Chen, et al., Enhanced broad band photodetection through piezo-phototronic effect in CdSe/ZnTe core/shell nanowire array, Adv. Electron. Mater. 1 (2015).
[51] G. Wang, Q. Sun, Y. Liu, et al., A bismuth-based metal-organic framework as an efficient visible-light-driven photocatalyst, Chemistry. 21 (2015) 2364–2367.
[52] F. Ye, Z.-X. Wei, J.-F. Song, et al., Synthesis, characterization, and photocatalytic properties of bismuth (III)-benzene-1,3,5-tricarboxylate, Z. Anorg. Allg. Chem. 643 (2017) 669–674.
[53] Y.-J. Kong, L.-J. Han, L.-T. Fan, et al., A bismuth-based fluorous metal-organic framework for efficient degradation of Congo red, J. Fluor. Chem. 186 (2016) 40–44.
[54] X. Zhang, S. Jiang, L.X. Sun, et al., Synthesis and structure of a 3D supramolecular layered Bi-MOF and its application in photocatalytic degradation of dyes, J. Mol. Struct. 1270 (2022), 133895.